CERES Terra/Aqua Edition4A SYN1deg Computed Fluxes – Accuracy and Validation

1.0 Accuracy and Validation

Generally, the uncertainty in monthly mean Ed4A SYN1deg computed surface fluxes are the same as monthly mean Ed4.0 EBAF-Surface fluxes. Uncertainties in surface fluxes at various temporal and special scales are estimated by Kato et al. (2017) and shown in Table 1. In addition to monthly mean flux uncertainties, root-mean-square differences of Ed4A SYN1deg and observed hourly mean fluxes (Figure 1) are used for the uncertainty of hourly mean fluxes (Table 1).

Table 1. Uncertainty (k=1 or 1σ) in Ed4.0 EBAF-Surface irradiances.

			Estimated uncertainty				
		Mean irradiance	Hourly gridded	Monthly gridded	Monthly zonal	Monthly global	Annual global
Downward longwave	Ocean+Land	345	21	7	6	5	5
	Ocean	364	20	5	5	5	5
	Land	333	24	10	9	5	5
	Arctic	183	-	12	-	-	-
	Antarctic	183	-	12	-	-	-
Upward longwave	Ocean+Land	398	-	15	8	3	3
	Ocean	402	-	13	9	5	5
	Land	394	-	19	15	5	4
	Arctic	219	-	12	-	-	-
	Antarctic	219	-	13	-	-	-
Downward shortwave	Ocean+Land	187	43	13	7	6	4
	Ocean	191	42	11	7	6	4
	Land	195	46	12	7	5	4
	Arctic	119	-	14	-	-	-
	Antarctic	119	-	21	-	-	-
Upward shortwave	Ocean+Land	23	-	11	3	3	3
	Ocean	12	-	11	3	3	3
	Land	53	-	12	8	6	6
	Arctic	86	-	16	-	-	-
	Antarctic	86	-	24	-	-	-

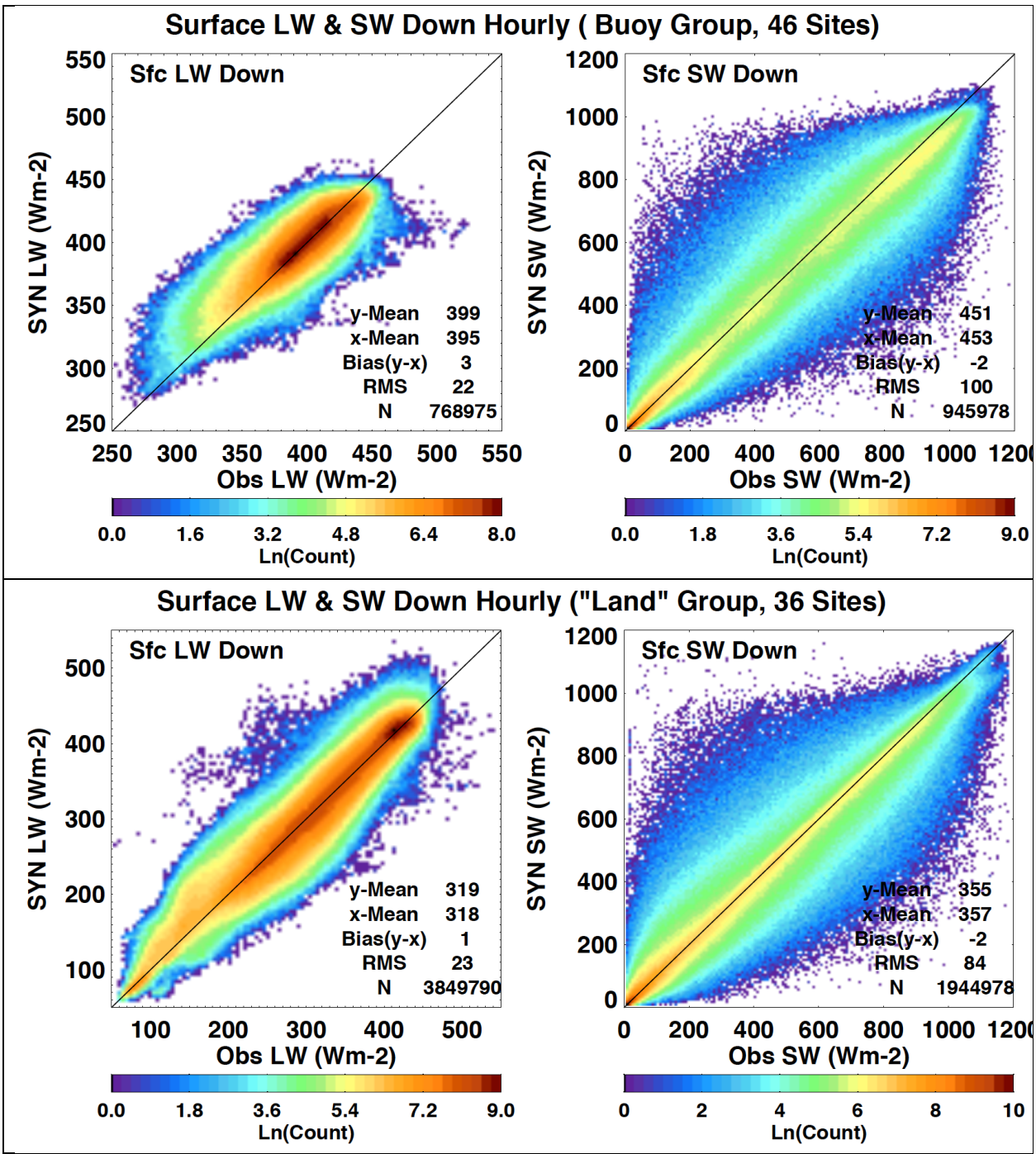

Figure 1. Ed4A SYN1deg hourly mean downward longwave (left) and shortwave (right) versus observed hourly mean fluxes for 16 buoys (top) and 27 land sites (bottom).

2.0 Regional Mean All-sky Surface Fluxes

The uncertainty in monthly mean downward fluxes are derived by comparing monthly mean irradiance at surface validation sites (Kato et al. 2017). The uncertainty in monthly mean upward fluxes are taken from Kato et al. (2013). The following sections summarize comparisons of monthly mean fluxes at buoys and land sites. Ed4.0 EBAF-Surface fluxes are used in the comparisons. Generally, the RMS difference of monthly mean Ed4.0 SYN1deg fluxes are similar to the RMS difference of monthly mean Ed4.0 EBAF-Surface fluxes.

3.0 Validation by Surface Observations

Figure 2 shows the difference of EBAF monthly 1°×1° mean surface (top) shortwave and (bottom) longwave downward fluxes from observed fluxes at buoys (computed minus observed). The mean difference on monthly mean fluxes averaged for 49 buoy sites is 4.9 W m^{-2} for downward shortwave and 1.1 W m^{-2} for downward longwave with the standard deviation of, respectively, 10.5 W m^{-2} and 4.7 W m^{-2}. Larger differences over tropical Atlantic ocean is caused by accumulation of dusts transported from Africa on buoys (Foltz et al. 2013). The bias of downward shortwave flux can exceed -40 W m^{-2} in a monthly mean for buoys located in the high-dust region (8°, 12°, and 15°N along 38°W; 12° and 21°N along 23°W), while mean bias is of the order of -10 W m^{-2}.

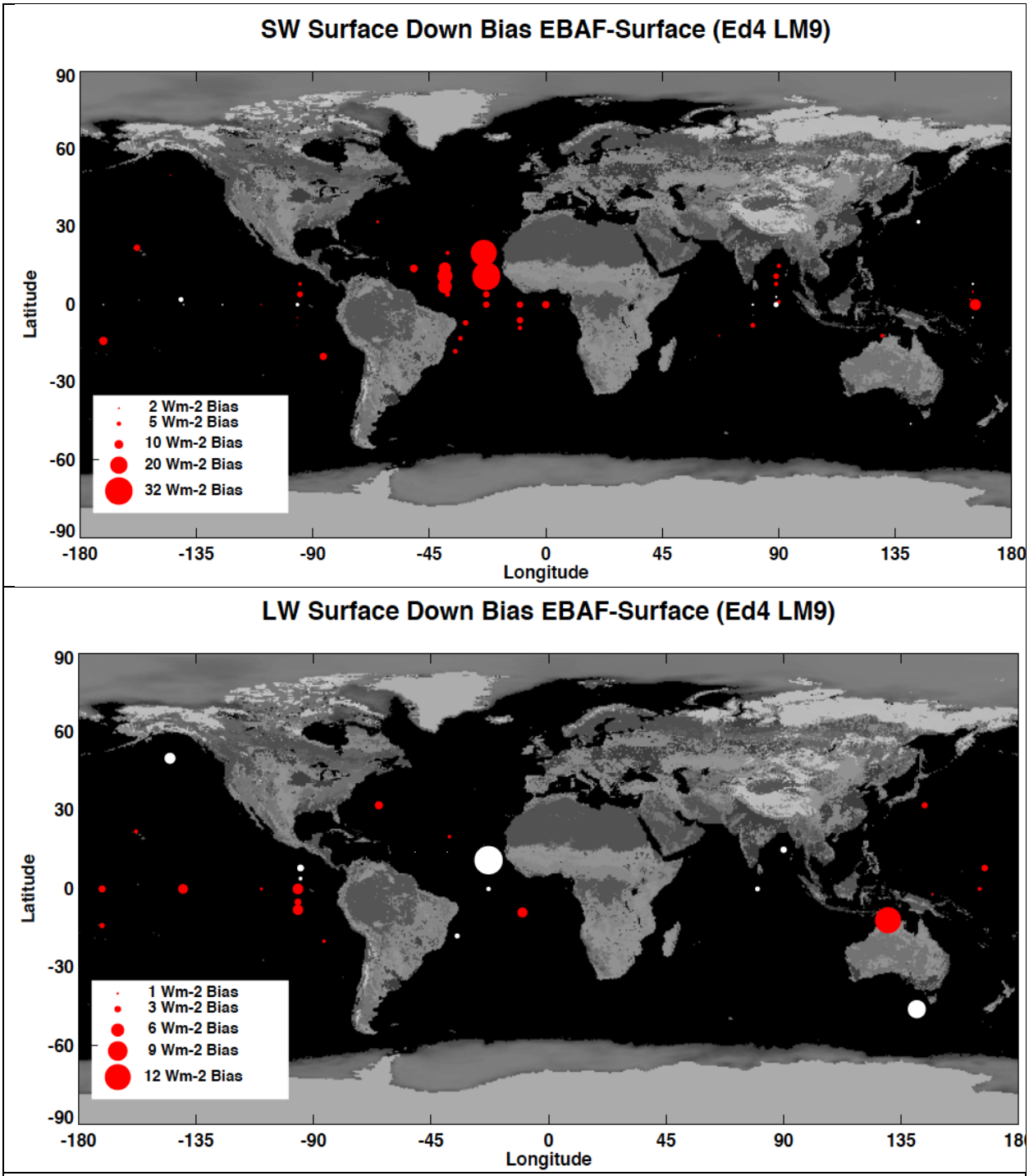

Figure 2. Difference of EBAF monthly 1°×1° mean surface (top) shortwave and (bottom) longwave downward fluxes from observed fluxes at buoys (computed minus observed). The size of the circle is proportional to the difference. The red and white circles indicate, respectively, a positive and a negative difference. The number of months used for comparisons varies depending on buoys.

Comparisons with surface observations by surface type are shown in in Table 2**.** Buoys in the tropical Atlantic ocean that have large biases due to African dust are excluded in computing the statistics shown in here.

Table 2. Difference in EBAF-Surface monthly 1°×1° mean downward shortwave and longwave fluxes (W m^{-2}) from surface observations. Numbers in parentheses are the standard deviations.

	Downward Shortwave	**Downward Longwave**
All sites (85 sites)	1.98 (12.64)	0.08 (9.21)
Ocean buoys	4.67 (10.65)	1.19 (4.84)
Land	-0.74 (11.59)	0.04 (9.76)
Arctic	3.74 (13.15)	0.43 (12.34)
Antarctic	-4.07 (20.13)	3.14 (11.73)

Comparison at Greenland sites

Downward surface shortwave fluxes are biased negative by 4 W m^{-2} and Downward surface longwave fluxes are biased positive by 11 W m^{-2} compared with observation taken at the Summit (SMT) (Figure 3). This is primarily due to a positive bias of cloud fraction over high elevation regions. In particular, low-mid and high-mid cloud fractions are biased high over the Summit site except for summer time. The effect of the positive bias of cloud fraction on surface radiative fluxes for other polar regions is less pronounced (Table 1).

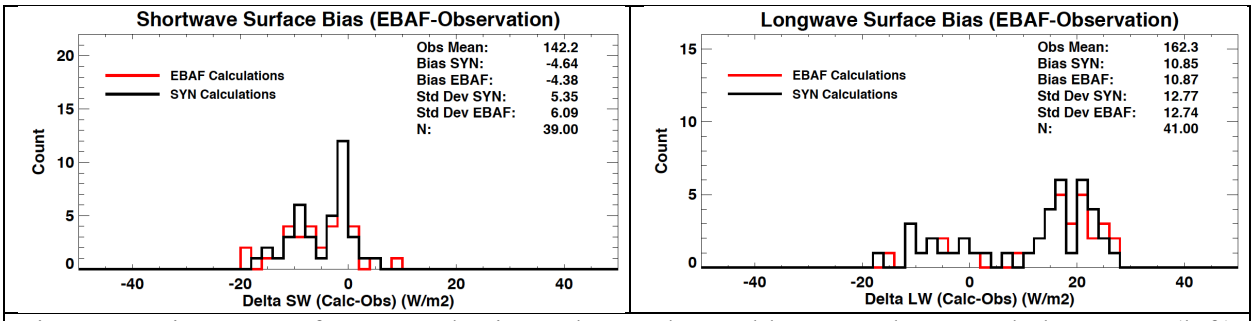

Figure 3. Histogram of computed minus observed monthly mean downward shortwave (left) and downward longwave (right) fluxes over the Greenland Summit site. Observed data are provided by Nate Miller.

4.0 Surface Longwave Flux During Polar Nights

Because of the degradation of Terra MODIS water vapor channel that is used to detect clouds mostly at high altitude in polar regions during polar nights, the nighttime cloud fraction over Antarctica derived from Terra MODIS is about 2% less than the nighttime cloud fraction derived from Aqua MODIS over the same region. The effect of the degradation on the surface downward longwave flux becomes apparent around 2008. A large drop of cloud fraction derived from Terra MODOS over the Antarctica occurs March 2016.

Because of the degradation of the Terra water vapor channel, the time series of downward longwave flux anomalies and net longwave flux anomalies over polar region (60N to 90N and 60S to 90S) shows downward trend (Figure 4). For this reason, trend analyses with surface fluxes over polar regions from Ed4.0 EBAF-Surface should be avoided.

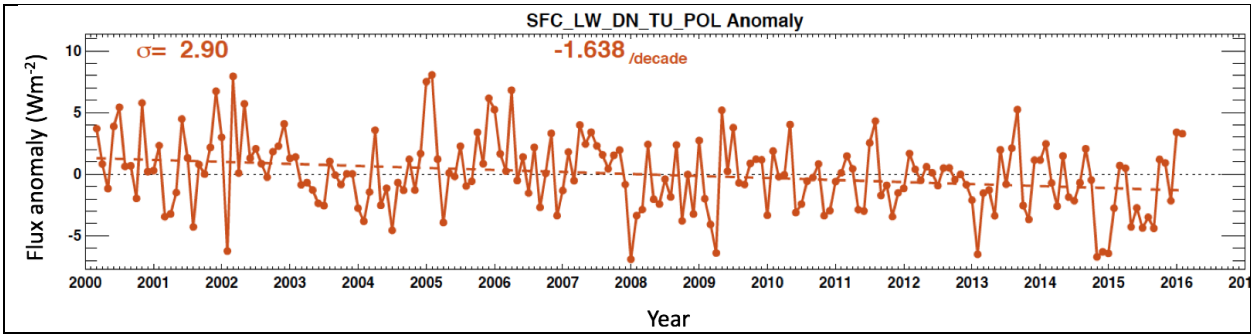

Figure 4. Time series of downward longwave flux anomalies over the Arctic (60°N - 90°N) and Antarctic (60°S – 90°S).

5.0 Entropy Production by Radiation

SYN1deg Ed4A provides entropy produced by radiative heating or cooling. Table 3 lists the entropy variables and formulas to compute them. The method to produce entropy productions is described in Kato and Rose (2020). A brief description of what is provided by SYN1deg product is given here.

When only heating and cooling processes are considered, entropy balance equation for the Earth system is (e.g. de Groot and Mazur, 1984; Bannon 2015; Bannon and Lee 2017),

$$\frac{dS}{dt} = \frac{Q_a}{T_a} - \frac{Q_e}{T_e} + \dot{\Sigma}_{\text{irr}} \qquad (1)$$

where $\frac{dS}{dt}$ is the rate of entropy change within the system, Q_a is heating due to absorption of shortwave irradiance, Q_e is cooling due to outgoing longwave irradiance, T_a is effective absorbing temperature, T_e is effective emission temperature, and $\dot{\Sigma}_{irr}$ is heating and colling due to irreversible processes. Irreversible processes include turbulent enthalpy transport, frictional dissipation, irreversible phase change, transport and precipitation of water, and frictional dissipation of falling raindrops, as well as heating and cooling due to radiation exchange within the Earth system (Kato and Rose 2020). Table 3 relates entropy variables provided by SYN1deg data product to terms of Eq. (1). The variable "atmos_entropy_gen_swnet" is entropy production by shortwave absorption within the atmosphere and "sfc_entropy_gen_swnet" is the entropy production by shortwave absorption by the surface. The sum of these two is $\frac{Q_a}{T_a}$. The variable "toa_out_entropy_lw" is the entropy carried by emitted longwave radiation at top-of-atmosphere, which is the sum of "atmos_out_entropy_lw" and "sfc_out_entropy_lw". "toa_out_entropy_lw" is 4/3 times $\frac{Q_e}{T_e}$. Therefore, "toa_out_entropy_lw" needs to be multiply by 3/4, ¾(toa_out_enytropy_lw)=$\frac{Q_e}{T_e}$.

As explained in (Gibbins and Haigh 2021), global annual mean $\frac{dS}{dt}$ should be nearly equal to the net TOA irradiance divided by the global annual mean ocean surface temperature because at an annual and global scale, energy absorbed by Earth is used to heat ocean (Johnson et al. 2015; von Schckmann 2020). Entropy production by irreversible processes can be estimated using Eq. (1). Because SYN1deg computed TOA net irradiance slightly differs from observed TOA net irradiance provided by EBAF, a scaling approach is recommended to derive $\dot{\Sigma}_{irr}$by

$$\dot{\Sigma}_{\mathrm{irr}} = -\frac{Q_{a,SYN}}{T_a}\frac{F^{net}_{TOA,SW\_EBAF}}{F^{net}_{TOA,SW\_SYN}} + \frac{Q_{e,SYN}}{T_e}\frac{F^{net}_{TOA,LW,EBAF}}{F^{net}_{TOA,LW,SYN}} + \frac{F^{net}_{TOA,SW+LW,EBAF}}{T_{skin}} \qquad (2)$$

Because entropy production is computed with adjusted irradiance (Rose et al. 2013), adjusted SYN irradiances need to be used for the scaling given by Eq. (2) (Gibbins and Haigh 2021). The eighteen year mean (March 2000 through February 2018) of $\dot{\Sigma}_{\mathrm{irr}} - \frac{dS}{dt}$ without scaling is 75.8 $\mathrm{mWm^{-2}\ K^{-1}}$ and with scaling is 80.4 $\mathrm{mWm^{-2}\ K^{-1}}$.

Entropy production by irreversible process within oceans is small (Bannon and Najjar 2018). If we ignore irreversible process within oceans, entropy production by irreversible processes excluding radiation exchange is the sum of "sfc_entropy_gen_swnet" and "sfc_entropy_gen_lwnet" multiplied by -1.

The entropy balance equation (1) can be applied to any temporal and spatial scales. However, when it is applied to a region, $\frac{dS}{dt}$ includes entropy storage dur to regional temperature change and $\dot{\Sigma}_{irr}$includes entropy produced by horizontal advection of dry static energy and kinetic energy. Because regional ocean heating rate is not known, using SYN1deg entropy variables, only regional $\frac{dS}{dt} - \dot{\Sigma}_{irr}$ and $\dot{\Sigma}_{irr}$ excluding entropy production by internal radiation exchange ($\dot{\Sigma}_{tur}$ in Kato and Rose 2020 and material entropy production in Gibbins and Haigh 2020) can be computed.

Table 3. Entropy generation by radiation provided by the SYN1deg Ed4A.

Variable Name	**Long Name**	**Formula**	**Note**
toa_in_entropy_sw	TOA Incoming Entropy (SW)	F_0(1-albedo)/T_{sun}	=atmos_in_entropy_sw + sfc_in_entropy_sw
atmos_in_entropy_sw	Atmosphere Incoming Entropy (SW)	Σ(Atm. SW absorbed)/T_{sun}	
sfc_in_entropy_sw	Surface Incoming Entropy (SW)	Σ(Sfc. Absorbed) / T_{sun}	
toa_out_entropy_lw	TOA Outgoing Entropy (LW)		=atmos_out_entropy_lw + sfc_out_entropy_lw Entropy flux $\frac{4}{3}\frac{Q_e}{T_e}$
atmos_out_entropy_lw	Atmosphere Outgoing Entropy (LW)	(4/3) Σ(LW emitted to space) / T_{layer}	Entropy flux $\frac{4}{3}\frac{Q_e}{T_e}$

Variable Name	Long Name	Formula	Note
sfc_out_entropy_lw	Surface Outgoing Entropy (LW)	(4/3) LW surface up emitted to space / T_{skin}	Entropy flux $\frac{4}{3}\frac{Q_e}{T_e}$
dn_sfc_entropy_lw	Downward Surface Entropy (LW)	(4/3) Σ(LW down at the surface) / T_{layer}	Entropy flux
atmos_entropy_gen_swnet	Atmosphere Entropy Generation by SW Net	Σ(SW net)/T_{layer}	$\frac{Q_a}{T_a}$
sfc_entropy_gen_swnet	Surface Entropy Generation by SW Net	SW absorbed by surface / T_{skin}	$\frac{Q_a}{T_a}$
up_sfc_entropy_lw	Upward Surface Entropy (LW)	(4/3) Σ(LW up at the surface) / T_{layer}	Entropy flux
atmos_entropy_gen_lwnet	Atmosphere Entropy Generation by LW Net	-(Σ(Atm. LW net) / T_{layer})	
sfc_entropy_gen_lwnet	Surface Entropy Generation by LW Net	-(Surface LW net /T_{skin})	

F_0 = downward shortwave flux at top-of-atmosphere
T_{sun} = temperature of the sun
T_{layer} = air temperature of atmospheric layers
T_{skin} = surface skin temperature

Annual global mean entropy production by radiation from Ed4A SYN1deg-Month is compared with values from Peixoto et al. (1991) and Stephens and O'Brien (1993) in Table 4.

Table 4. Absolute value of annual global mean entropy production in mW m^{-2} K^{-1}.

Entropy	SYN1deg-Month Ed4A	Peixoto et al. (1991)	Stephens and O'Brien (1993)
TOA incoming SW	41	41.3	
Atmosphere incoming SW	13		
Surface incoming SW	28		
TOA outgoing LW	1238*		1230*
Atmosphere outgoing LW	827	854	
Surface outgoing LW	115	71	
Surface downward LW	1602		
Atmosphere absorbed SW	303	258	
Surface absorbed SW	549	29.5	
Surface upward LW	1784		
Atmosphere absorbed LW	729	24	

Entropy	SYN1deg-Month Ed4A	Peixoto et al. (1991)	Stephens and O'Brien (1993)
Surface absorbed LW	173	236	

* Entropy flux, which includes (4/3) factor.

6.0 2004 Aerosol Optical Thickness Issue

Aerosol optical thicknesses that are used for assimilation in the MATCH aerosol transport model are a combination of dark target (Levy et al. 2013) and deep blue (Hsu et al. 2006). Generally, dark target aerosol optical thicknesses are used over ocean and deep blue aerosol optical thicknesses are used over land. Regions where both dark target and deep blue aerosol optical thicknesses are available, an arithmetic mean of optical thickness derived from both algorithms is used. Terra-only aerosol optical thicknesses are used from March 2000 through June 2002, and Terra + Aqua from July 2002 onward. Aerosol optical thicknesses derived from the Terra dark target are generally larger than those derived from Aqua dark target and those derived from Terra and Aqua deep blue algorithms.

Because of a bug in a code, only Aqua aerosol optical thicknesses are used from July 2004 through December 2004. The global mean aerosol optical thickness of this 6-month period is 0.006 to 0.009 smaller than the Terra + Aqua aerosol optical thickness. The aerosol optical thickness problem affects computed clear-sky fluxes. Figure 5 shows the regional distribution of clear flux differences for October 2004 when the global mean aerosol optical thickness difference is the largest among differences in the 6-month period. The global mean aerosol optical thickness, TOA and surface flux differences are shown in Table 5.

Table 5. Global mean difference of aerosol optical thickness and clear-sky fluxes. Numbers in parentheses are the standard deviations of 1°×1° values in the month.

Year Month	Global mean difference (Terra + Aqua) – Aqua only		
	Aerosol optical thickness	Clear-sky surface downward flux	Clear-sky TOA reflected shortwave flux
2004 07	0.0058 (0.010)	-0.406 (0.685)	0.144 (0.254)
2004 08	0.0068 (0.011)	-0.455 (0.767)	0.158 (0.242)
2004 09	0.0080 (0.010)	-0.521 (0.614)	0.197 (0.219)
2004 10	0.0091 (0.011)	-0.617 (0.694)	0.228 (0.237)
2004 11	0.0086 (0.010)	-0.566 (0.661)	0.224 (0.239)
2004 12	0.0074 (0.010)	-0.497 (0.679)	0.208 (0.239)

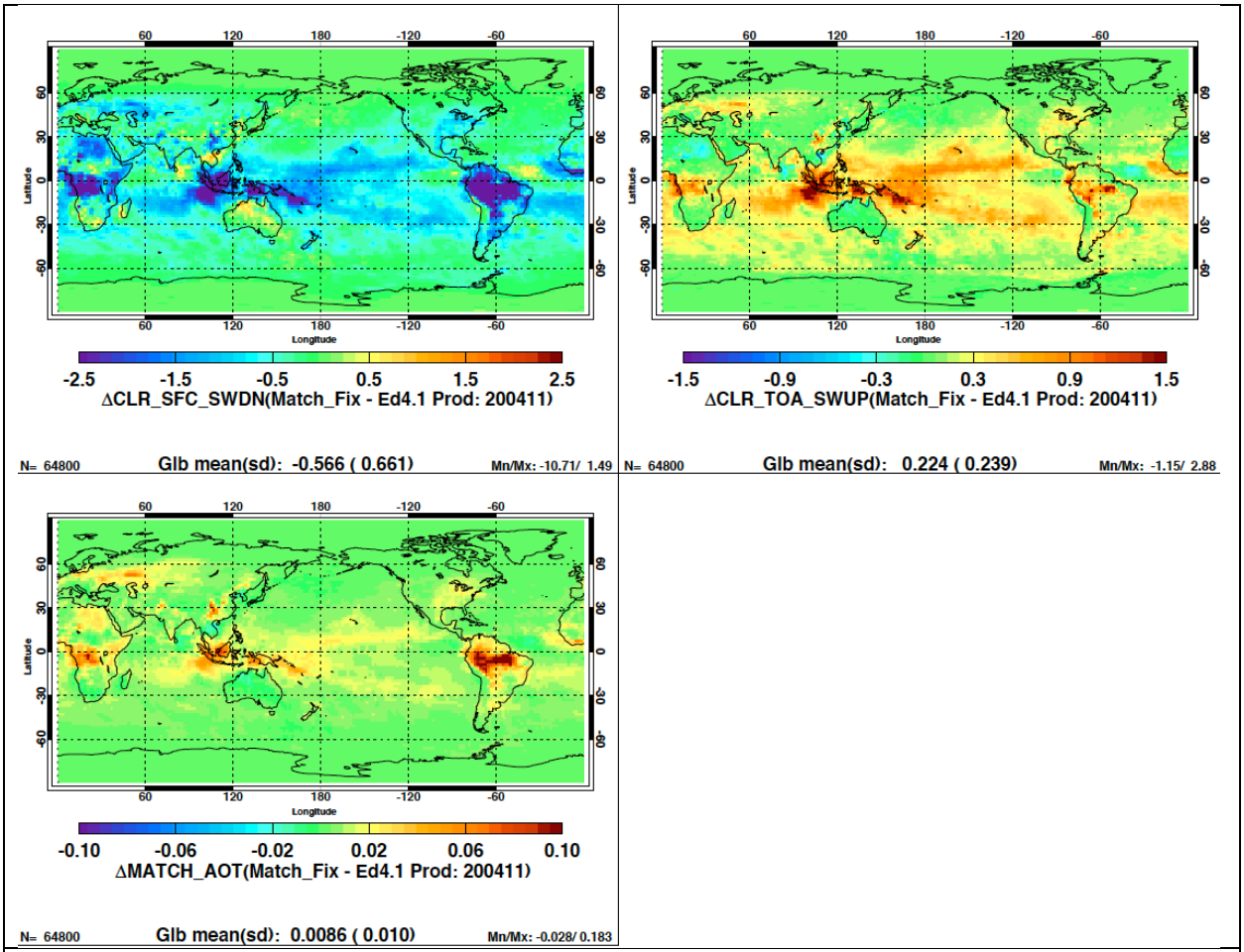

Figure 5. Difference of (top left) computed clear-sky surface downward shortwave fluxes, (top right) computed clear-sky top-of-atmosphere reflected shortwave fluxes, and (bottom) aerosol optical thicknesses for October 2004. The differences are Terra + Aqua aerosol optical thickness – Aqua only aerosol optical thickness for the bottom plot and computed fluxes with them for the top two plots.

7.0 Surface Longwave Irradiance Anomaly Timeseries

Cloud properties derived from new generation geostationary satellites such as Himawari-8, GOES-16, and GOES-17 are different from those derived from older geostationary satellites. For example, the cloud fraction is slightly larger and the cloud base height is higher because more channels are used for the retrievals and they are sensitive to optically thinner clouds. The difference in nighttime cloud properties is larger than the difference in daytime cloud properties. As a consequence, as new generation geostationary satellites replace older geostationary satellites, nighttime downward longwave irradiances computed with cloud properties derived from new generation geostationary satellites are smaller than those derived from older geostationary satellites (Kato et al. 2020). The operational periods of geostationary satellites are shown on https://ceres.larc.nasa.gov/data/general-product-info/#ceres-input-data-sources. Because surface temperature increases with time, the global downward longwave irradiance anomaly time series does not show a significant downward trend because increasing near surface

temperature (Figure 6). However, net longwave irradiance time series show a significant downward trend (Figure 7).

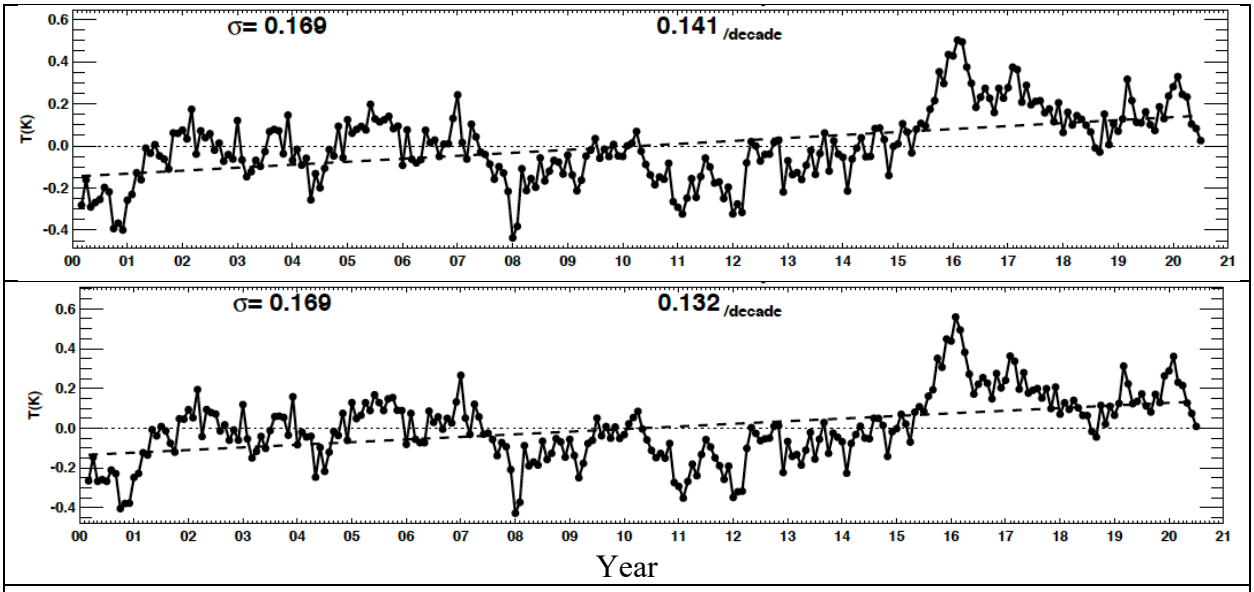

Figure 6. Time series of (top) global monthly surface temperature anomalies and (bottom) air temperature anomalies.

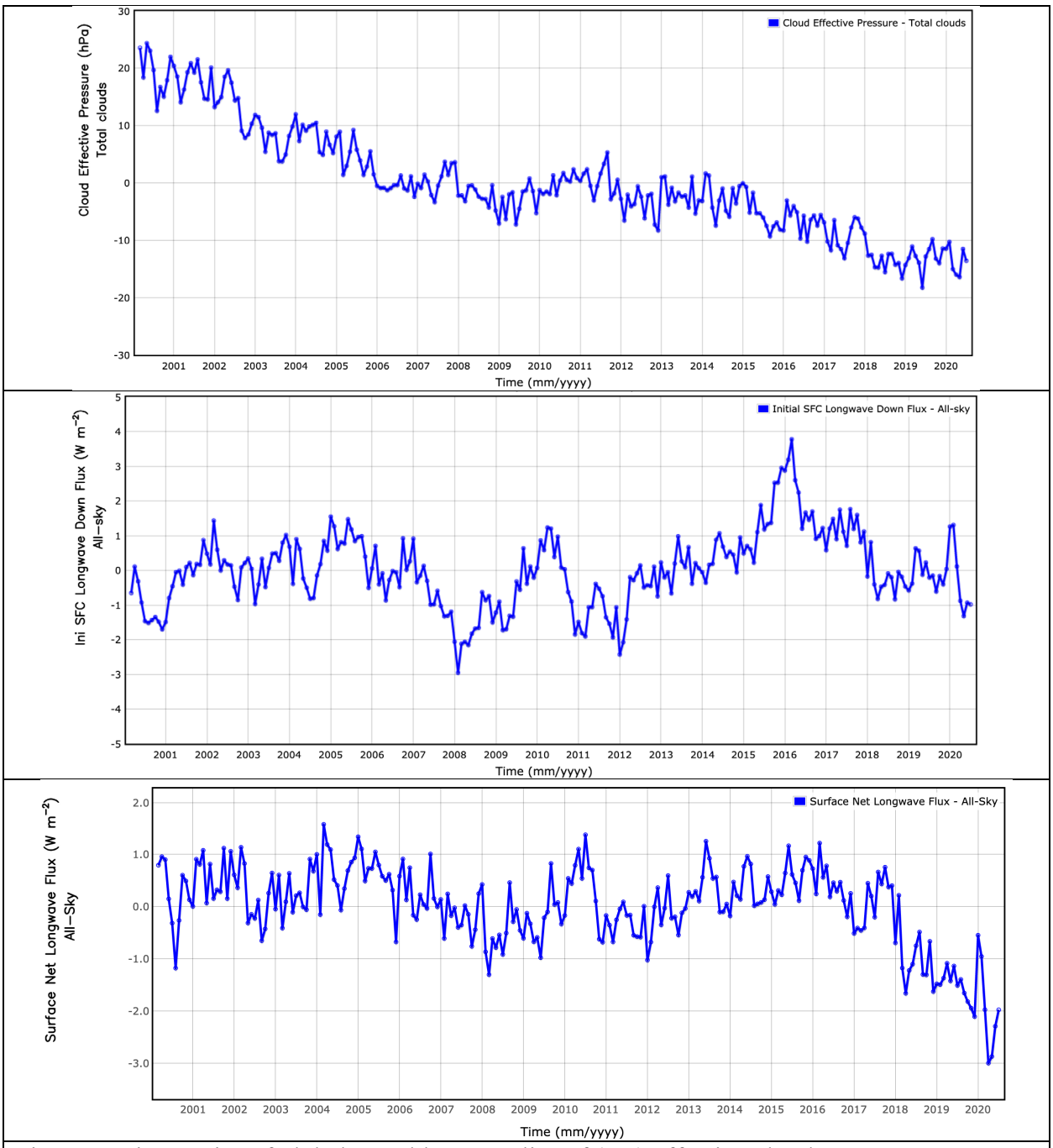

Figure 7. Time series of global monthly anomalies of (top) effective cloud top pressure (day+night), (middle) downward surface longwave irradiance, and (bottom) surface net longwave irradiance.

References

Bannon, P. R., 2015: Entropy production and climate efficiency, J. Atmos. Sci., 72, doi:10.1175/JAS-D-14-0361.1.

Bannon, P. R., and S. Lee, 2017; Toward quantifying the climate heat engine: Solar absorption and terrestrial emission temperature and material entropy production, J. Atmos. Sci, 74, doi:10.1175/JAS-D-16-0240.1.

Bannon, P. R., and Najjar, R. G., 2018: Heat-engine and entropy-production analyses of the world ocean. *Journal of Geophysical Research: Oceans*, *123* 8532–8547. https://doi.org/10.1029/2018JC014261

de Groot, S. R., and P. Mazur, 1984: Non-equilibrium thermodynamics, Dover Publications, inc.

Gibbins, G, and J. D. Haigh, 2021: Comments on "Global and regional entropy production by radiation estimated from satellite observations", *J. Climate*., 34, 3721-3728, doi:0.1175/JCLI-D-20-0685.1.

Gibbins, G., J. D. Haigh, 2020: Entropy production rates of the climate, J. Atmos. Sci., doi:10.1175/JAS-D-19-0294.1.

Hsu, N. C., S.-C. Tsay, M. D. King, J. R. Herman, 2006: Deep blue retrievals of Asian aerosol properties during ACE-Asia, IEEE Trans. Geosc. Remote Sens. 44, 11 3180-3195.

Johnson, G. C., J. M. Lyman, and N. G. Loeb, 2016: Improving estimates of Earth's energy imbalance. Nat. Climate Change, 6, 639–640, DOI: 10.1038/nclimate3043.

Kato, S., N. G. Loeb, F. G. Rose, D. R. Doelling, D. A. Rutan, T. E. Caldwell, L. Yu, and R. A. Weller, 2013: Surface irradiances consistent with CERES-derived top-of-atmosphere shortwave and longwave irradiances, *J. Climate*, **26**, 2719-2740, doi:10.1175/JCLI-D-12-00436.1.

Kato, S., and F. G. Rose, 2021: Reply to "Comments on 'Global and regional entropy production by radiation estimated from satellite observations'", *J. Climate*., 34, 3729-3731, doi:0.1175/JCLI-D-20-0950.1.

Kato, S., and F. G. Rose, 2020: Global and Regional Entropy Production by Radiation Estimated from Satellite Observations. *J. Climate*, **33**, 2985–3000, doi:10.1175/JCLI-D-19-0596.1.

Levy, R. C., S. Matto, L. A. Munchak, L. A. Remer, A. M. Sayer, F. Patadia, and N. C. Hsu, 2013: The collection 6 MODIS aerosol products over land and ocean, Atmos. Meas. Tech., 6, 2989–3034, doi:10.5194/amt-6-2989-2013.

Rose, F. G., D. A. Rutan, T. Charlock, G. L. Smith, and S. Kato, 2013: An algorithm for the constraining of radiative transfer calculations to CERES-observed broadband top-of-atmosphere irradiance, J. Atmos. Ocean. Technol., 30, 1091-1106, DOI: 10.1175/JTECH-D-12-00058.1.

Von Schuckmann, K., and coauthors, 2020: Heat stored in the Earth system: where does the energy go?, Earth Syst. Sci. Data, 12, 2013-2041, doi:10.5149/essd-12-2013-2020.